Observation of flat bands due to band hybridization in the 3*d*-electron heavy-fermion compound $CaCu_3Ru_4O_{12}$

Haijiang Liu,[1,2] Yingying Cao,[1,2] Yuanji Xu,[1,2] D. J. Gawryluk,[3,*] E. Pomjakushina,[3] S.-Y. Gao,[1,2] Pavel Dudin,[4] M. Shi,[5] Lei Yan,[1] Yi-feng Yang,[1,2,6,†] and H. Ding[1,2,6,‡]

[1]*Beijing National Laboratory for Condensed Matter Physics and Institute of Physics, Chinese Academy of Sciences, Beijing 100190, China*
[2]*School of Physical Sciences, University of Chinese Academy of Sciences, Beijing 100190, China*
[3]*Laboratory for Multiscale Materials Experiments, Paul Scherrer Institute, Villigen CH-5232, Switzerland*
[4]*Diamond Light Source, Harwell Science and Innovation Campus, Didcot OX11 0DE, England, United Kingdom*
[5]*Swiss Light Source, Paul Scherrer Institute, CH-5232 Villigen PSI, Switzerland*
[6]*Songshan Lake Materials Laboratory, Dongguan, Guangdong 523808, China*

(Received 4 February 2020; revised 23 April 2020; accepted 17 June 2020; published 6 July 2020)

We report angle-resolved photoemission spectroscopy and first-principles numerical calculations for the band-structure evolution of the 3*d* heavy-fermion compound $CaCu_3Ru_4O_{12}$. Below $T \sim 200$ K, we observed an emergent hybridization gap between the Cu 3*d*-electron-like band and the Ru 4*d*-hole-like band and the resulting flat band features near the Fermi level centered around the Brillouin-zone corner. Our results confirm the non-Kondo nature of the $CaCu_3Ru_4O_{12}$, in which the Cu $3d_{xy}$ electrons are less correlated and not in the Kondo limit. Comparison between theory and experiment also suggests that other mechanisms may be needed to give a full quantitative explanation of the peculiar properties in this material.

DOI: 10.1103/PhysRevB.102.035111

I. INTRODUCTION

Heavy-fermion materials are mostly intermetallics with partially filled $4f$ or $5f$ orbitals [1], except for a few examples of 3*d*-electron systems that include LiV_2O_4, $FeGe_3Te_2$, $CaCu_3Ir_4O_{12}$, etc [2–7]. The mechanism underlying these 3*d* heavy-fermion materials remains unclear. Among them, the *A*-site ordered perovskite $ACu_3B_4O_{12}$ (A = Ca, La, Na; B = Ru, Ir) provides a highly tunable platform for investigating the heavy-fermion properties and mechanism with the perovskite-type structure. $CaCu_3Ru_4O_{12}$ (CCRO) is the earliest member studied in this family. It has an electronic specific-heat coefficient of about 84 $mJ/(mol\,K^2)$ [8], which is much larger than that of a normal metal. The enhanced Sommerfeld coefficient was initially attributed to the Kondo physics of the Cu localized 3*d* moments due to a similar magnetic susceptibility behavior with the classical $4f$ electron heavy-fermion material $CeSn_3$ [8]. Indeed a broad maximum feature was observed in the magnetic susceptibility around $T \sim$ 180–200 K, which was originally identified as the Kondo temperature. Photoemission data [9] also suggested that CCRO is a Kondo system due to the observation of a resonancelike peak at E_F albeit without momentum-resolved data. However, a later nuclear magnetic resonance (NMR) experiment up to 700 K observed no signatures of the local moment [10], thus posing a severe challenge to the Kondo scenario. A two-band model was later proposed to explain the NMR results. The broad maximum feature was then explained as a consequence of a peak in the density of states (DOS) just above the Fermi level [11]. In fact, the origins of this broad maximum may also include low-dimensional spin correlations, spin frustration, excitation from spin-singlet to spin-triplet states, Kondo effect, pseudogap, and metamagnetic nature of itinerant electrons in CCRO. So far, no decisive conclusions have been reached on the mechanism of these unusual properties, in particular, their correspondence with the electronic band structures at the microscopic level.

In this paper, we performed a systematic electronic structure study on CCRO by using angle-resolved photoemission spectroscopy (ARPES) and density functional theory (DFT) calculations in combination with the dynamical mean-field theory (DMFT) for local Coulomb interactions of the Cu 3*d* orbitals. By tracking carefully the temperature evolution of low-energy electronic structure, we are able to reveal two nearly flat bands near the Fermi level emerging below $T \sim$ 200 K as a result of hybridization between the Cu 3*d*-electron-like band and the Ru 4*d*-hole-like band. At temperatures above $T \sim$ 200 K, the hybridization diminished, but the Cu $3d_{xy}$ band still remains near the Fermi level, which is in strong contrast to the usual Kondo picture and indicates the more itinerant and non-Kondo nature of the Cu 3*d* electrons in this compound. Our detailed DFT+DMFT calculations confirm the observed band structures but predict a crossover at much higher temperature, implying the presence of other possible mechanisms such as nonlocal interactions or spin fluctuations beyond local correlation. Comparison between experiment and theory suggests that a two-band correlated model, in which the Cu $3d_{xy}$ electrons are not in the Kondo limit, may be needed. These results provide important information for clarifying the origin of the heavy-fermion properties in CCRO

*On leave from Institute of Physics, Polish Academy of Sciences, Aleja Lotnikow 32/46, Warsaw PL-02-668, Poland.
†Corresponding author: yifeng@iphy.ac.cn
‡Corresponding author: dingh@iphy.ac.cn

and will also promote our understanding of other members of this family.

The $CaCu_3Ru_4O_{12}$ single crystals used in this paper were grown by the flux method at the Paul Scherrer Institut of Switzerland. The starting materials were CuO (99.995%, Alfa Aesar), RuO_2 (99.9%, chemPUR), and $CaCO_3$ (99.997%, Alfa Aesar). RuO_2 was dried in air at 900 °C for 12 h, and then cooled to 150 °C. $CaCO_3$, CuO, and freshly dried RuO_2 were mixed together in the molar ratio of 1:33:4, respectively, and placed into a platinum crucible. Here, the excess of CuO acts as a flux. The crucible with the starting reagents was heated in air to 1000 °C at 400 °C/h for 3 h, further heated to 1175 °C at 60 °C/h for 12 h, and then cooled to 1075 °C at 1 °C/h, after which they were furnace cooled to the room temperature. The excess of CuO flux was removed by washing the resulted specimen with 1M HCl.

The magnetic susceptibility was measured by using a vibrating sample magnetometer from $T = 5$ to 300 K with an external magnetic field of $H = 1$ T. Electrical resistivity and heat capacity were measured by a standard Physical Property Measurement System from Quantum Design. The specific heat was measured using a standard relaxation method from $T = 2$ to 80 K. The resistivity was measured using the four probe method from $T = 2$ to 300 K. Contacts for resistivity were made by silver paste. For heat-capacity measurement, several pieces of single crystals were selected and put together to have enough mass.

II. RESULTS AND DISCUSSIONS

In order to confirm the expected structure, laboratory powder x-ray-diffraction patterns were collected at room temperature in the Bragg-Brentano (θ-2θ) geometry in the angle range $5° < 2\theta < 120°$ with steps of 0.02° and averaging time of 1 s/step using a Bruker AXS D8 Advance diffractometer (Bruker AXS GmbH) equipped with a Ni-filtered Cu Kα radiation and a one-dimensional LynxEye PSD detector. The samples (12 powdered crystals) were spread with Vaseline on a silicon (low background) sample holder, which were rotating during the measurement (with a rotational speed of 15 rpm). All the reflections were indexed with a perovskite-related cubic cell in the space group *Im*-3 (no. 204). The Rietveld refinement analysis [12] of the diffraction patterns was performed with the package FULLPROF SUITE [13,14] (version November 2019) using a previously determined instrument resolution function (based on the small linewidth polycrystalline sample $Na_2Ca_3Al_2F_{14}$ measurements [15,16]). The structural model was taken from the published data based on single-crystal x-ray-diffraction data analysis [17]. Refined parameters were scale factor; zero shift; lattice parameters; isotropic thermal displacement of Ca, Cu, and Ru atoms; and peak shapes with the Thompson-Cox-Hastings pseudo-Voigt function. Due to the habit of powdered crystals, a preferred orientation as a March-Dollase multiaxial phenomenological model was implemented in the analysis. Determined lattice parameters are $a = b = c = 7.420\,18(1)$ Å. R_{wp}, R_P, R_{exp} Bragg R factor, Rf factor, χ^2, and GoF (not corrected for background) were, respectively, 4.55, 2.55, 1.93, 3.40, 3.04, 5.57, and 2.3 in the final Rietveld refinement.

High-quality single crystals of CCRO were cleaved *in situ* along the (001) plane at $T = 15$ K with the vacuum below 5×10^{-11} mbar. Three-dimensional visualization of CCRO crystal structure was generated by the VESTA software [18] as shown in the inset of Fig. 1(a). CCRO adopts the ABO_3 perovskite-type crystal structure. The Ca and Cu ions are located at the *A* site surrounded by 12 nearest oxygen ions (small red ball). The Ru ions occupy the *B* site surrounded by six nearest oxygen ions forming an octahedron. The first Brillouin zone is shown in the inset of Fig. 1(c) with the length of Γ-H of 0.85 $Å^{-1}$. The Fermi surface in the (001) plane is the same as that of the (100) and (010) planes due to the high symmetry of the lattice structure. ARPES measurements were carried out at the SIS beamline of Swiss Light Source using a SCIENTA R4000 analyzer and at the I05 beamline at the Diamond light source using a SCIENTA R4000 analyzer. Figure 1(b) displays the wide range valence-band spectrum obtained with photon energy $h\nu = 122$ eV. Three main features can be observed around −5, −2.6, and −0.1 eV, and are attributed to the O 2*p*, Cu 3*d,* and Ru 4*d* states, as they are consistent with a previous bulk PES experiment [19] and numerical calculations [20].

Apart from the powder XRD and PES characterization, transport data are more sensitive to small off-stoichiometry, which might have influence on the absence of Kondo behavior of CCRO. Figure 1(d) shows the magnetic susceptibility of the CCRO single crystal from $T = 5$ to 300 K. A characteristic broad maximum around $T \sim 200$ K is observed which is in agreement with previous measurements [8,21]. The heat capacity $C(T)/T$ vs T of CCRO is shown in Fig. 1(e), exhibiting a conventional behavior of metallic Fermi liquids for $T > 2$ K. As shown in the inset of Fig. 1(e), $C(T)/T$ of CCRO is plotted as a function of T^2, which shows the relation $C(T)/T = \gamma + \beta T^2$, as is expected for the Fermi liquid below $T < 25$ K. We obtained a similar electron specific-heat coefficient $\gamma = 26.2 \pm 0.9$ mJ/mol Cu K^2, which is in agreement with previous reports [8,21,22]. Figure 1(f) shows the electrical resistivity of CCRO single crystal from $T = 2$ to 300 K. Metallic behavior is observed in the entire temperature range with a quadratic temperature dependence $\rho = \rho_0 + AT^2$ for $T < 30$ K, characteristic of a Fermi liquid, as illustrated in the inset of Fig. 1(f). The residual resistivity is $\rho_0 = 18.98\,\mu\Omega$ cm and the coefficient is $A = 4.97 \times 10^{-9}\,\Omega\,\mathrm{cm/K^2}$.

To reveal the highly three-dimensional band structure of CCRO, we performed a photon energy dependent measurement with photon energies from 25 to 161 eV in steps of 2 eV with the circular polarization along a single cut along the Γ-H direction at $T = 15$ K, as shown in Fig. 2(a). From the obvious periodicity of the Fermi surface and the cut along the k_z direction, we estimated the inner potential of $V_0 = 13$ eV. From comparison with the calculations, we assign the intense point in Fig. 2(a) to the H point and the faint point to the Γ point. Correspondingly, the photon energies crossing the Γ or H point are 61, 95, and 122 eV, as shown in Fig. 2(a). The three cuts cross the high-symmetry Γ or H point along the Γ-H path measured at corresponding photon energies, and as shown in Figs. 2(b)–2(d), clearly reveal a flat band feature near the Fermi level with high intensity centered at the H point, which could be the origin of heavy electrons in this material. In order to show the clear Fermi surface in the Γ-H-N

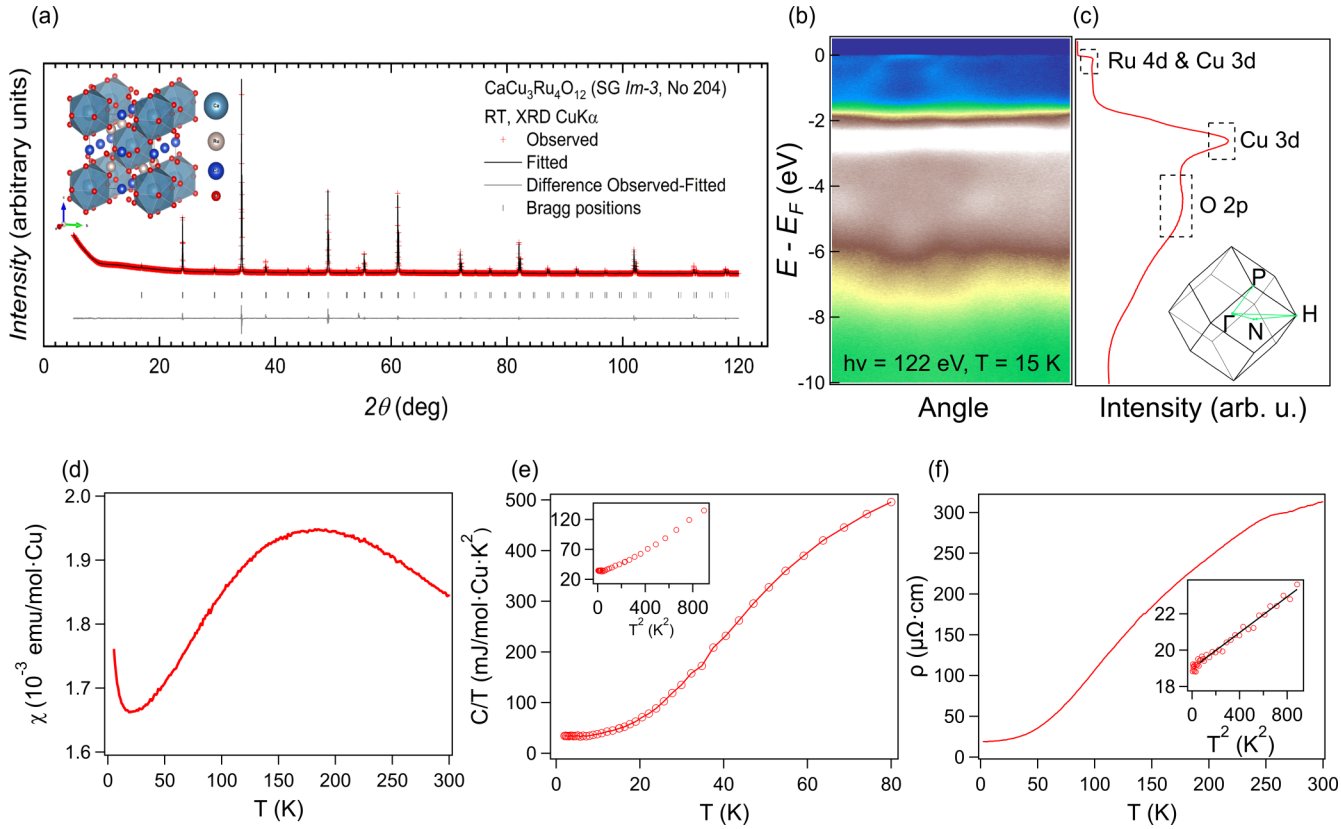

FIG. 1. Characterization of $CaCu_3Ru_4O_{12}$. (a) Laboratory x-ray powder diffraction (Cu Kα radiation, room temperature) pattern (red crosses) of $CaCu_3Ru_4O_{12}$ powdered crystals. The black line corresponds to the best fit from the Rietveld refinement. Lower vertical marks denote the Bragg peak positions. The bottom line represents the difference between experimental and calculated points. (b) Valence-band spectrum of $CaCu_3Ru_4O_{12}$. (c) Integrated density of states of (b) and the first Brillouin zone of body centered cubic (bcc). (d) Magnetic susceptibility measured with a magnetic field $H = 1$ T. (e) Specific heat of CCRO. (f) Electrical resistivity of CCRO.

plane, we display the Fermi surface measured with the photon energy $h\nu = 122$ eV at $T = 6$ K with the circular polarization in Fig. 2(e). The Fermi-surface map shows obvious strong intensity centered at the H point.

To better understand the cause of this flat band, we carried out temperature-dependent measurements along the Γ-H direction. We chose the photon energy $h\nu = 122$ eV which has a high contrast at the H point. As mentioned above, previous magnetic susceptibility measurements show a broad maximum feature around $T \sim 200$ K, which is the crossover temperature. Figures 3(a)–3(f) plot the symmetric spectra from $T = 270$ to 52 K covering the crossover regime. At $T = 270$ K, one can see a holelike band and an electronlike band centered at the H point. Comparison with first-principles calculations suggests that the holelike band is composed of the Ru 4*d* orbital, while the electronlike band comes mainly from the Cu 3*d* orbital. With decreasing temperature across $T \sim 200$ K, the spectral intensity at the bottom of the Cu 3*d*-electron band becomes stronger and starts to hybridize with the Ru 4*d*-hole band, forming an M-shape hybridized

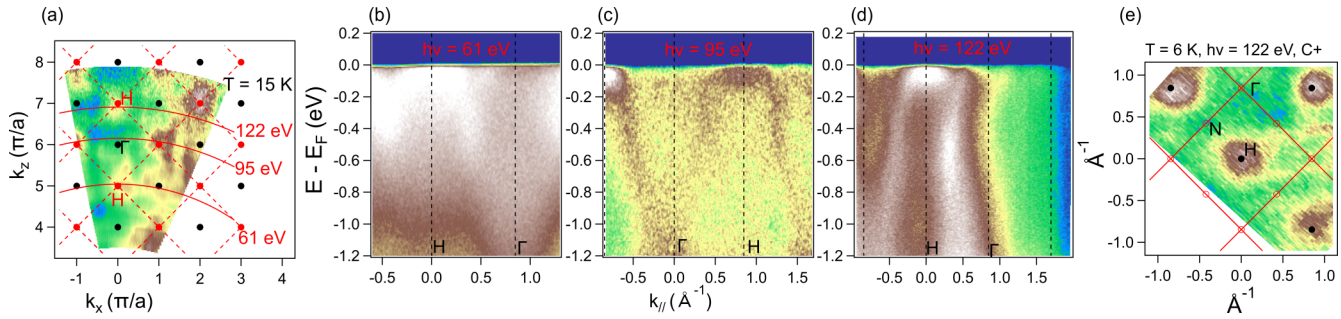

FIG. 2. k_z map, several high-symmetry cuts, and in-plane Fermi surface measured with $h\nu = 122$ eV. (a) k_z map obtained from $h\nu = 25$ to 161 eV in steps of 2 eV at a low temperature of 15 K with circular polarization. Red dashed grids are the Brillouin-zone boundary of the *ac* plane. Γ-H cuts with photon energies at (b) 61 eV, (c) 95 eV, and (d) 122 eV. Inner potential $V_0 = 13$ eV was estimated from k_z dispersions. (e) Fermi surface measured with photon energy $h\nu = 122$ eV at $T = 6$ K with circular polarization.

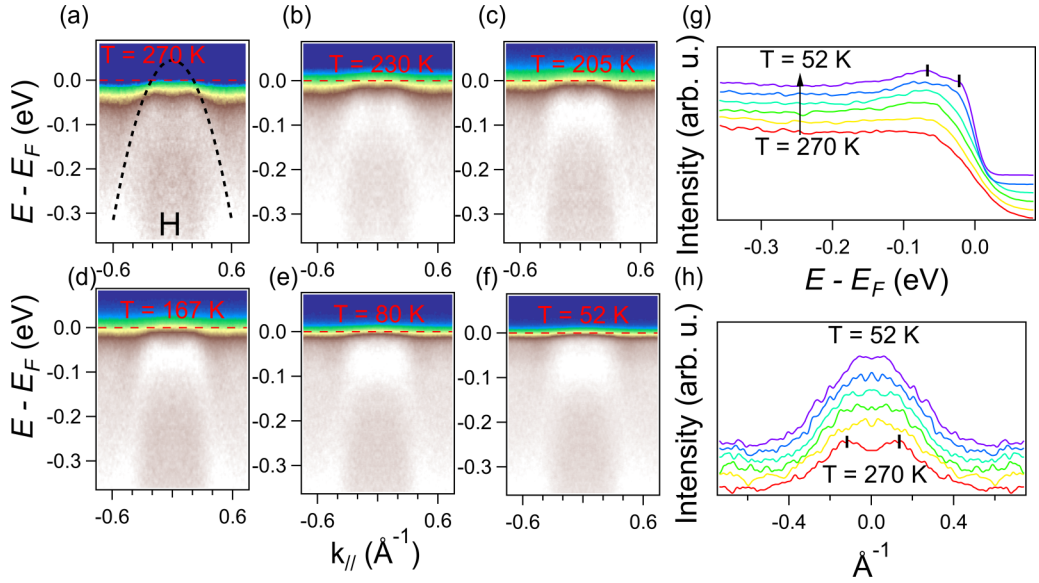

FIG. 3. Temperature dependence of band structure around the H point. (a–f) Spectra around the H point at corresponding temperatures. (g) EDCs at the H point. (h) MDCs at the Fermi level. The parabolic dashed line in (a) indicates the hole band across the Fermi level at $T = 270$ K. Two short vertical bars in (g) indicate two quasiparticle peaks near the Fermi level at $T = 52$ K. Two short vertical bars in (h) indicate the k_Fs of the hole band at $T = 270$ K.

band below the Fermi level. In Fig. 3(g), the energy distribution curve (EDC) at the H point at $T = 52$ K shows two peaks derived from the upper and lower hybridization bands. From the temperature-dependent momentum distribution curves (MDCs) in Fig. 3(h), the peaks residing at around ± 0.15 Å^{-1} at high temperature shrink, indicating the momenta change due to the hybridization between Ru 4*d* and Cu 3*d* electrons.

More information on the band hybridization can be obtained by dividing the measured spectra with the resolution-convoluted Fermi-Dirac function. The Fermi level and the overall experiment energy resolution were fitted in a low-temperature spectrum, and the overall energy resolution is about 22 meV. This resolution is reasonably good at this photon energy to achieve a good signal-noise ratio. As shown in Fig. 4, the Ru 4*d*-hole pocket and Cu 3*d*-electron pocket seem to cross the Fermi level without hybridization at high temperatures above $T \sim 200$ K. When the sample is cooled down, the two bands start to hybridize, forming an M-shape feature around the H point. At $T = 52$ K, both of the hybridized bands are intensive with little dispersion around the H point. The EDCs in Fig. 4(g) are chosen at $k = 0$, where we can clearly identify two peaks at $T = 52$ K around -68 and 22 meV, showing a gap of about 90 meV. The EDCs at $k \approx 0.15$ Å^{-1} in Fig. 4(h) show similar features. We think our conclusion is convincing and reliable due to the fact that the noise level is much lower than the value itself below $E_F + 34$ meV as shown in Figs. 4(g) and 4(h).

III. THEORETICAL CALCULATIONS

To understand the origin of the band hybridization, we carried out first-principles calculations combining DFT and DMFT [23–26]. The DFT part was computed using the full-potential linearized augmented plane-wave method implemented in the WIEN2K package [27,28]. We considered non-spin-polarized calculations for CCRO with the lattice parameter $a = 7.4082$ Å. The O atomic position was set to be (0, 0.1782, 0.3053) with the muffin-tin radii (R_{MT}) of 1.70 a.u. for O, 1.99 a.u. for Ru, 1.97 a.u. for Cu, and 2.46 a.u. for Ca. We took 2000 **k** points in the Brillouin zone and $R_{\mathrm{MT}}K_{\mathrm{max}} = 8.0$. In the DMFT part, the Cu $3d_{\mathrm{xy}}$ bands were considered as correlated orbitals. The double-counting term of the self-energy function was estimated by the nominal scheme. The electron correlation of the Cu $3d_{\mathrm{xy}}$ orbitals was treated within the one-shot scheme using the hybridization expansion continuous-time quantum Monte Carlo (CT-HYB) as the impurity solver [29]. The DMFT calculation was performed with more than 5×10^7 CT-HYB steps per processor and more than 20 processors were used for adequately high accuracy. To obtain spectral functions, the maximum entropy method was used for analytic continuation of the self-energy [30].

Figure 5 summarizes our major results from the DFT+DMFT calculations with a very large Coulomb interaction $U = 12$ eV. For clarity, we first compare in Fig. 5(a) the derived Cu $3d_{\mathrm{xy}}$ bands at 50 K with the DFT bands. We see an overall renormalization factor of about 0.5 on the bandwidth due to electronic correlations, as indicated by the arrow. Figure 5(b) plots the partial DOS of the Cu 3*d* orbitals at 50 and 1000 K in a larger energy window. We see that all other Cu 3*d* orbitals are fully occupied and located at 2–3 eV below the Fermi level, while only the $3d_{\mathrm{xy}}$ orbitals are partially occupied and play a role near the Fermi level. Interestingly, we observe two Hubbard peaks and the quasiparticle peak at both temperatures. But as the temperature increases, all peaks change only slightly, implying that the quasiparticle peak cannot originate from the Kondo hybridization. This indicates that the Cu $3d_{\mathrm{xy}}$ electrons are not fully localized even at high temperatures and the compound is not in the Kondo limit.

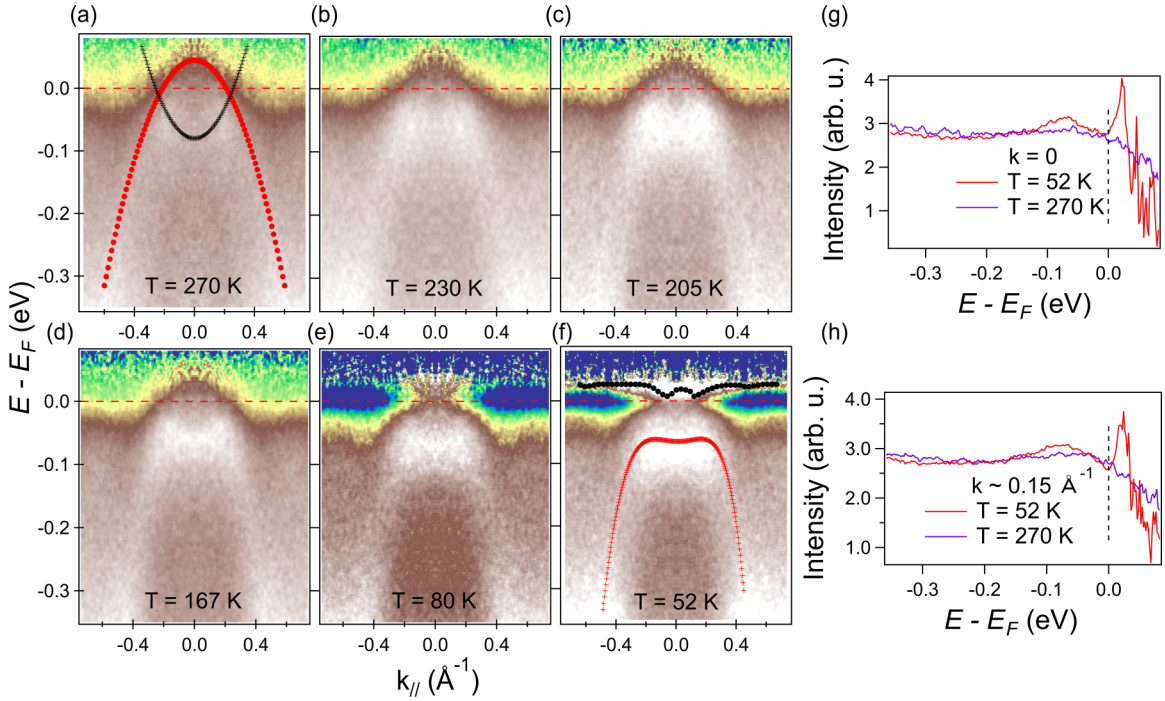

FIG. 4. Spectra divided by the resolution-convoluted Fermi-Dirac function to obtain the information above E_F at corresponding temperatures. EDCs at $T = 52$ and 270 K at (g) $k = 0$ and (h) $k \sim 0.15$ Å^{-1}.

The degree of renormalization increases with increasing U. However, we find that a very large U beyond 12 eV is needed in order to make comparison with experiment, suggesting the possibility of nonlocal correlations or strong spin fluctuations that may help to enhance the band renormalization in real materials [11]. One may also include the Coulomb interaction on the dispersive and partially occupied Ru 4d bands. Our preliminary results reveal no qualitative change in the conclusion but suggest that a fine tuning of the parameters might lead to a somewhat better comparison with experiment by renormalizing slightly the Ru 4d bands. We leave this for future elaboration and focus here on the qualitative picture.

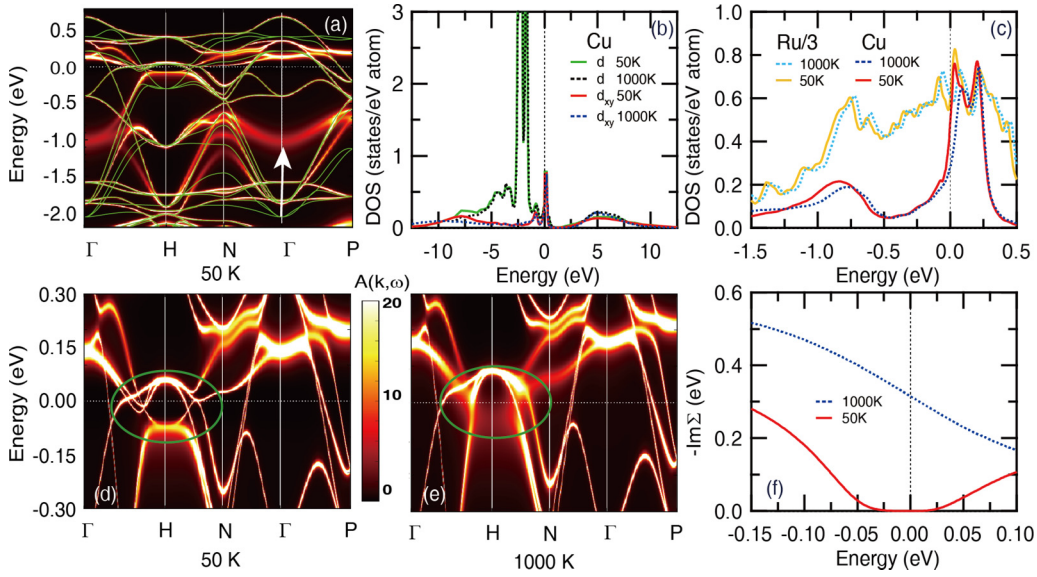

FIG. 5. (a) DFT+DMFT spectral functions along the Γ-H-N-Γ-P path at 50 K. The DFT bands (green lines) are also plotted for comparison. The white arrow indicates the renormalization effect due to electronic correlation. (b) The partial DOS of Cu 3d (green and black) and Cu 3d_{xy} (red and blue) at 50 K (solid lines) and 1000 K (dashed lines). (c) The partial DOS of Cu 3d_{xy} (red and blue) and Ru 4d divided by 3 (yellow and cyan) at 50 and 1000 K showing the quasiparticle peak between −1.5 and 0.5 eV. (d, e) Comparison of DFT+DMFT spectral functions at 1000 and 50 K in a smaller energy window. Green circles mark the hybridization effect around the H point. (f) The imaginary part of self-energy at 50 and 1000 K for the Cu 3d_{xy} orbital.

To clarify the nature of the quasiparticle peak, we plot and compare it with the Ru $4d$ DOS in a smaller energy window in Fig. 5(c), where it splits into several small peaks. The two peaks above the Fermi level and the one at about -0.8 eV exist at all temperatures for both Ru $4d$ and Cu $3d_{xy}$ orbitals. This indicates that the Cu $3d_{xy}$ bands also exist at high temperature and these peaks probably originate from the usual band hybridization between the two itinerant bands. There is an additional peak below the Fermi level at around -0.08 eV. At high temperature, it seems to be present only for the Ru $4d$ DOS. Thus, it cannot come from the hybridization but should be from the Ru $4d$ bands themselves. However, at $T = 50$ K, a tiny peak appears at roughly the same location in the Cu $3d_{xy}$ DOS, suggesting the presence of hybridization at low temperature.

To understand this, we further plot in Figs. 5(d) and 5(e) the DFT+DMFT band structures in an even smaller energy window. At high temperature [Fig. 5(e)], the Cu $3d_{xy}$ band becomes almost smeared out, and the Ru $4d$ bands cross the Fermi level around the H point, as observed in ARPES, while at low temperature, when the three Cu $3d_{xy}$ bands are less broadened, the Ru $4d$ bands are bent around the H point by the hybridization from -0.08 eV up to the Fermi level. The presence of the flat band at around -0.08 eV is in qualitative agreement with experiment at low temperature. However, we can only obtain the crossover at a much higher temperature beyond 200 K. Our calculated DOS only yields about half of the experimental Sommerfeld coefficient at zero temperature. Both indicate the presence of other correlation effects beyond the single site DMFT. We may therefore have underestimated the hybridization effect near the Fermi level. In our calculations, because the Ru $4d$ DOS per unit cell is about four times that of the Cu $3d_{xy}$ electrons, the overall DOS is still dominated by the Ru $4d$ contribution and the hybridization at low temperature only causes a slight shift of the dip and the peaks in the DOS.

Summing up, we may conclude that the temperature change of the band structures around the Fermi level is different from that of the usual Ce-based heavy-fermion compounds and should be attributed to the change of the $3d_{xy}$ band broadening. As shown in Fig. 5(f), there is indeed a large increase of the imaginary part of the Cu $3d_{xy}$ self-energy with increasing temperature. The suppression of the flat band at -0.08 eV is therefore a result of diminishing hybridization as the $3d_{xy}$ electrons become less coherent with increasing temperature. To see this, we may write down the dispersions of the hybridization bands as

$$E_{k,\pm} = 1/2[\varepsilon_{k,1} + \varepsilon_{k,2} - i\Gamma \pm ((\varepsilon_{k,1} - \varepsilon_{k,2} - i\Gamma)^2 + 4V^2)^{1/2}],$$

where $\varepsilon_{k,1}$ and $\varepsilon_{k,2}$ are the dispersions of the Cu $3d_{xy}$ and Ru $4d$ bands, respectively; Γ is the imaginary part of the Cu $3d_{xy}$ self-energy; and V is the effective hybridization. For $\Gamma \ll V$, these give rise to well-defined hybridization bands. But for $\Gamma \gg V$, we have approximately the expansion, $E_{k,+} = \varepsilon_{k,1} - i(\Gamma - V^2/\Gamma)$ and $E_{k,-} = \varepsilon_{k,2} - iV^2/\Gamma$, such that the two bands are effectively decoupled. Indeed, we see at high temperatures a hole band from the Ru $4d$ orbital and a weak electron band from the Cu $3d$ orbital around the H point.

Thus we have a good qualitative agreement between the experiment and calculations, which confirms the presence of a flat hybridization band around the H point. However, unlike the usual Kondo lattice, the Cu $3d$ electrons remain itinerant at high temperatures. This clearly rules out the Kondo scenario and implies a different mechanism in this compound. Our observation is consistent with the absence of local magnetic moment revealed by NMR [10] and supports the two-band scenario from the moderately correlated electrons (Cu $3d_{xy}$) and itinerant holes (Ru $4d$). Note that one should not intend to explain all the details based on the current numerical calculations, which may have ignored some other important correlation effects. In fact, the relatively weak renormalization effect might be responsible for the discrepancies in the Sommerfeld coefficient, the crossover temperature, and the exact location of the DOS peaks.

IV. CONCLUSIONS

To summarize, we performed ARPES measurements and first-principles calculations on the $3d$-electron perovskite-type heavy-fermion $CaCu_3Ru_4O_{12}$. The itinerant Cu $3d$-electron band hybridizes with the Ru $4d$-hole band, opens a hybridization gap near the H point, and forms a flat band below the Fermi level below $T \sim 200$ K. Our results exclude the Kondo scenario in $CaCu_3Ru_4O_{12}$, and suggest that some other mechanisms beyond the Kondo scenario such as a two-band model may be needed to explain the mechanism of the heavy-fermion $CaCu_3Ru_4O_{12}$.

ACKNOWLEDGMENTS

This work was supported by the National Key Research and Development Program of China (Grants No. 2016YFA0401000 and No. 2017YFA0303103) and the National Natural Science Foundation of China (Grants No. 11674371, No. 11974397, and No. 11774401).

[1] G. R. Stewart, Heavy-fermion systems, Rev. Mod. Phys. **56**, 755 (1984).

[2] S. Kondo, D. C. Johnston, C. A. Swenson, F. Borsa, A. V. Mahajan, L. L. Miller, T. Gu, A. I. Goldman, M. B. Maple, D. A. Gajewski, E. J. Freeman, N. R. Dilley, R. P. Dickey, J. Merrin, K. Kojima, G. M. Luke, Y. J. Uemura, O. Chmaissem, and J. D. Jorgensen, LiV_2O_4: A Heavy Fermion Transition Metal Oxide, Phys. Rev. Lett. **78**, 3729 (1997).

[3] R. Arita, K. Held, A. V. Lukoyanov, and V. I. Anisimov, Doped Mott Insulator as the Origin of Heavy-Fermion Behavior in LiV_2O_4, Phys. Rev. Lett. **98**, 166402 (2007).

[4] Y. Shimizu, H. Takeda, M. Tanaka, M. Itoh, S. Niitaka, and H. Takagi, An orbital-selective spin liquid in a frustrated heavy fermion spinel LiV_2O_4, Nat. Commun. **3**, 981 (2012).

[5] K. Tomiyasu, K. Iwasa, H. Ueda, S. Niitaka, H. Takagi, S. Ohira-Kawamura, T. Kikuchi, Y. Inamura, K. Nakajima, and

K. Yamada, Spin-Orbit Fluctuations in Frustrated Heavy-Fermion Metal LiV_2O_4, Phys. Rev. Lett. **113**, 236402 (2014).

[6] Y. Zhang, H.-Y. Lu, X.-G. Zhu, S.-Y. Tan, W. Feng, Q. Liu, W. Zhang, Q.-Y. Chen, Yi Liu, X.-B. Luo, D.-H. Xie, L.-Z. Luo, Z.-J. Zhang, and X.-C. Lai, Emergence of Kondo lattice behavior in a van der Waals itinerant ferromagnet, Fe_3GeTe_2, Sci. Adv. **4**, eaao6791 (2018).

[7] J. G. Cheng, J. S. Zhou, Y. F. Yang, H. D. Zhou, K. Matsubayashi, Y. Uwatoko, A. MacDonald, and J. B. Goodenough, Possible Kondo Physics Near a Metal-Insulator Crossover in the A-Site Ordered Perovskite $CaCu_3Ir_4O_{12}$, Phys. Rev. Lett. **111**, 176403 (2013).

[8] W. Kobayashi, I. Terasaki, J.-I. Takeya, I. Tsukada, and Y. Ando, A novel heavy-fermion state in $CaCu_3Ru_4O_{12}$, J. Phys. Soc. Jpn. **73**, 2373 (2004).

[9] T. Sudayama, Y. Wakisaka, K. Takubo, T. Mizokawa, W. Kobayashi, I. Terasaki, S. Tanaka, Y. Maeno, M. Arita, H. Namatame, and M. Taniguchi, Bulk-sensitive photoemission study of $ACu_3Ru_4O_{12}$ (A = Ca, Na, and La) with heavy-fermion behavior, Phys. Rev. B **80**, 075113 (2009).

[10] H. Kato, T. Tsuruta, M. Matsumura, T. Nishioka, H. Sakai, Yo Tokunaga, S. Kambe, and R. E. Walstedt, Temperature-induced change in the magnitude of the effective density of states: A NQR/NMR study of the A-site-ordered perovskite system $CaCu_3Ru_4O_{12}$, J. Phys. Soc. Jpn. **78**, 054707 (2009).

[11] T.-H. Kao, H. Sakurai, S. Yu, H. Kato, N. Tsujii, and H.-D. Yang, Origin of the magnetic susceptibility maximum in $CaCu_3Ru_4O_{12}$ and electronic states in the A-site substituted compounds, Phys. Rev. B **96**, 024402 (2017).

[12] H. M. Rietveld, A profile refinement method for nuclear and magnetic structures, J. Appl. Cryst. **2**, 65 (1969).

[13] J. Rodríguez-Carvajal, Recent advances in magnetic structure determination by neutron powder diffraction, Physica B **192**, 55 (1993).

[14] T. Roisnel and J. Rodríguez-Carvajal, WinPLOTR: A windows tool for powder diffraction patterns analysis, Mat. Sci. Forum **378**, 118 (2001).

[15] F. Gozzo, L. De Caro, C. Giannini, A. Guagliardi, B. Schmitt, and A. Prodi, The instrumental resolution function of synchrotron radiation powder diffractometers in the presence of focusing optics, J. Appl. Cryst. **39**, 347 (2006).

[16] G. Courbion and G. Ferey, $Na_2Ca_3Al_2F_{14}$: A new example of a structure with "independent F^-"—A new method of comparison between fluorides and oxides of different formula, J. Solid State Chem. **76**, 426 (1988).

[17] M. A. Subramanian and A. W. Sleight, $ACu_3Ti_4O_{12}$ and $ACu_3Ru_4O_{12}$ perovskites: High dielectric constants and valence degeneracy, Solid State Sci. **4**, 347 (2002).

[18] K. Momma and F. Izumi, VESTA 3 for three-dimensional visualization of crystal, volumetric and morphology data, J. Appl. Crystallogr. **44**, 1272 (2011).

[19] T. T. Tran, K. Takubo, T. Mizokawa, W. Kobayashi, and I. Terasaki, Electronic structure of $CaCu_3Ru_4O_{12}$ studied by x-ray photoemission spectroscopy, Phys. Rev. B **73**, 193105 (2006).

[20] H.-P. Xiang, X.-J. Liu, E.-J. Zhao, J. Meng, and Z.-J. Wu, First-principles study on the conducting mechanism of the heavy-fermion system $CaCu_3Ru_4O_{12}$, Phys. Rev. B **76**, 155103 (2007).

[21] A. Krimmel, A. Günther, W. Kraetschmer, H. Dekinger, N. Büttgen, A. Loidl, S. G. Ebbinghaus, E. W. Scheidt, and W. Scherer, Non-Fermi-liquid behavior in $CaCu_3Ru_4O_{12}$, Phys. Rev. B **78**, 165126 (2008).

[22] R.-J. Wang, Y.-Y. Zhu, L. Wang, Y. Liu, J. Shi, R. Xiong, and J.-F. Wang, Growth and characterization of $CaCu_3Ru_4O_{12}$ single crystal, Chin. Phys. B **24**, 097501 (2015).

[23] G. Kotliar, S. Y. Savrasov, K. Haule, V. S. Oudovenko, O. Parcollet, and C. A. Marianetti, Electronic structure calculations with dynamical mean-field theory, Rev. Mod. Phys. **78**, 865 (2006).

[24] A. Georges, G. Kotliar, W. Krauth, and M. J. Rozenberg, Dynamical mean-field theory of strongly correlated fermion systems and the limit of infinite dimensions, Rev. Mod. Phys. **68**, 13 (1996).

[25] K. Haule, C. H. Yee, and K. Kim, Dynamical mean-field theory within the full-potential methods: Electronic structure of $CeIrIn_5$, $CeCoIn_5$, and $CeRhIn_5$, Phys. Rev. B **81**, 195107 (2010).

[26] K. Held, O. K. Andersen, M. Feldbacher, A. Yamasaki, and Y.-F. Yang, Bandstructure meets many-body theory: The LDA+DMFT method, J. Phys.: Condens. Matter **20**, 064202 (2008).

[27] P. Blaha, K. Schwarz, G. Madsen, D. Kvasnicka, and J. Luitz, WIEN2K, An Augmented Plane Wave+Local Orbitals Program for Calculating Crystal Properties, Karlheinz Schwarz, Technische Universität, Wien, Austria, 2014.

[28] J. P. Perdew, K. Burke, and M. Ernzerhof, Generalized Gradient Approximation Made Simple, Phys. Rev. Lett. **77**, 3865 (1996).

[29] E. Gull, A. J. Millis, A. I. Lichtenstein, A. N. Rubtsov, M. Troyer, and P. Werner, Continuous-time Monte Carlo methods for quantum impurity models, Rev. Mod. Phys. **83**, 349 (2011).

[30] J.-H. Sim and M. J. Han, Maximum quantum entropy method, Phys. Rev. B **98**, 205102 (2018).